

Tailoring Third-Harmonic Diffraction Efficiency by Hybrid Modes in High-Q Metasurfaces

Kirill I. Okhlopkov,* Attilio Zilli, Andrea Tognazzi, Davide Rocco, Luca Fagiani, Erfan Mafakheri, Monica Bollani, Marco Finazzi, Michele Celebrano, Maxim R. Shcherbakov, Costantino De Angelis, and Andrey A. Fedyanin



Cite This: *Nano Lett.* 2021, 21, 10438–10445



Read Online

ACCESS |



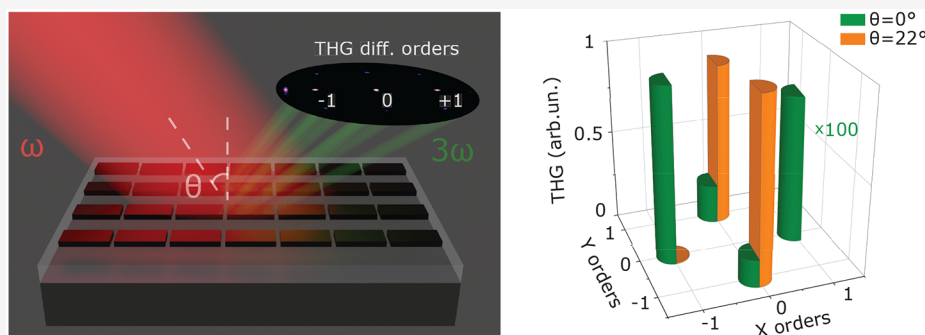
Metrics & More



Article Recommendations



Supporting Information



ABSTRACT: Metasurfaces are versatile tools for manipulating light; however, they have received little attention as devices for the efficient control of nonlinearly diffracted light. Here, we demonstrate nonlinear wavefront control through third-harmonic generation (THG) beaming into diffraction orders with efficiency tuned by excitation of hybrid Mie–quasi-bound states in the continuum (BIC) modes in a silicon metasurface. Simultaneous excitation of the high-Q collective Mie-type modes and quasi-BIC modes leads to their hybridization and results in a local electric field redistribution. We probe the hybrid mode by measuring far-field patterns of THG and observe the strong switching between $(0, -1)$ and $(-1, 0)$ THG diffraction orders from 1:6 for off-resonant excitation to 129:1 for the hybrid mode excitation, showing tremendous contrast in controlling the nonlinear diffraction patterns. Our results pave the way to the realization of metasurfaces for novel light sources, telecommunications, and quantum photonics.

KEYWORDS: *Third-harmonic diffraction, all-dielectric metasurface, high-Q metasurface, wavefront control, hybrid mode, bound states in the continuum*

When light interacts with a periodic structure with a pitch larger than the wavelength, light diffraction occurs. The nonlinear interactions of light with media lead to a wide class of phenomena associated with the nonlinear diffraction of light. Nonlinear diffraction was originally reported for second-harmonic generation (SHG) in systems with periodic spatial modulation of the quadratic susceptibility $\chi^{(2)}$.¹ The nonlinear diffraction of SHG and third-harmonic generation (THG) was further demonstrated for various periodic systems including 2D^{2–4} and 3D nonlinear photonic crystals.^{5,6} In these systems, second or third harmonics were generated efficiently as the nonlinear Bragg law was fulfilled at the quasi-phase matching condition. Diffraction is also actively studied in metasurfaces, 2D arrays of subwavelength nanoresonators, which allow one to manipulate the phase, amplitude, and polarization of transmitted or reflected light by engineering the constituent elements (i.e., meta-atoms).⁷ On-demand control of the diffraction efficiency has been demonstrated through specifi-

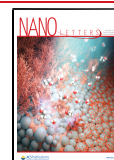
cally designed spatial phase gradients realized for both plasmonic^{8,9} and dielectric metasurfaces.^{7,10–13}

The use of materials with large nonlinear susceptibilities expands the operation scope of metasurfaces to the nonlinear signals. The employment of materials with a high-refractive index¹⁴ for metasurfaces further boosts the nonlinear-optical effects in visible and near-IR ranges due to the strong local field enhancement inside the nanoresonators.^{15–21} Moreover, metasurfaces allow one to control the nonlinear wavefront^{22–24} and, in particular, the nonlinear diffraction^{25–28} through size,

Received: September 30, 2021

Revised: November 19, 2021

Published: December 7, 2021



shape, and orientation engineering of meta-atoms even in the absence of phase matching.

Nonlinear diffraction in metasurfaces strongly depends on the local field distribution, which is controlled through resonant modes, in particular, Mie-type resonances of individual meta-atoms^{15,29} or bound states in the continuum (BIC) resonances.^{30–33} Collective resonances of many adjacent meta-atoms give an additional boost of electric field localization^{34,35} and leads to the appearance of Fano lineshapes^{36,37} due to the interference of the narrow (high-Q) lattice resonance with a broad spectrum, paving the way to new functionalities for wavefront manipulations, nonlinear diffraction control, and light–matter interactions.

Here, we realize an all-dielectric metasurface supporting hybrid Mie–quasi-BIC modes at telecommunication wavelengths and demonstrate its capability to control the third-harmonic (TH) diffraction through the switching between TH diffraction orders. The local electric field enhancement at a wavelength close to 1554 nm is obtained by breaking the translation invariance of a waveguide array; this leads to the excitation of hybrid Mie–quasi-BIC modes, which result in strong THG. By varying the incident pump beam angle, we demonstrate the modification of the local electric field in the meta-atoms leading to the switching between THG diffraction orders.

The studied metasurface is a 2D array of nominally identical rectangular silicon cuboids.^{38,39} Because of the high refractive index, negligible absorption, and large third-order susceptibility of silicon at telecommunication wavelengths, the metasurface can significantly enhance the nonlinear optical effects under resonant excitation. The system was designed as a square array of cuboids with an aspect ratio of approximately 2:1 and similar periods along the two orthogonal in-plane axes to realize the high-Q collective resonances⁴⁰ (Figure 1a,b). The elongated shape of nanoresonators plays a key role in the dependence of the metasurface response on the direction of incident linear polarization.³⁸ The use of laser radiation at a wavelength of 1554 nm as the pump leads to THG at a wavelength of 518 nm for which the metasurface itself is a diffraction grating. The emitted THG signal is diffracted in a

square pattern with nine equidistant diffraction orders (see Figures 1a and 3a).

The metasurface was fabricated out of a silicon-on-insulator (SOI) wafer by electron-beam lithography and reactive-ion etching (see Methods). The thickness of the top silicon layer was 125 nm, and the thickness of the buried SiO₂ layer of the SOI wafer was 2 μm . The metasurface spans a square area of 25 \times 25 μm^2 . The periods of cuboids along the x and y axes were almost identical, being 1065 and 1060 nm, respectively (see Figure 1b). The length and the width of the cuboids were chosen to be 940 and 428 nm, respectively.³⁹

Such metasurface features both Mie-type modes and a quasi-BIC mode, which hybridize at the condition of spectral overlapping. To study in detail the angular dispersion of these modes, we carried out angle-resolved calculations of the transmittance spectra for two orthogonal exciting polarizations across and along the long side of the cuboid. The angle of incidence was tilted away from normal in a S-polarized configuration to maintain the exciting field parallel to the metasurface plane. The sketches of polarizations, cross-S and co-S, with denoted angles of incidence, θ_1 and θ_2 , are represented in Figure 2a,b. In cross-S polarization, for a normal incidence around 1585 nm, we observe a narrow Fano feature, which is associated with the interference of a Mie-type magnetic quadrupole (MQ) mode with a broad Fabry–Pérot resonance inside the SiO₂ substrate (see Figure 2c). Due to the odd number of local electric field nodes along the long side of the cuboid, the MQ mode has odd parity and mirror symmetry and can be resolved at normal incidence. The magnetic dipole (MD) mode has even parity, an even number of local electric field nodes along the long side of the cuboids, and cannot be resolved at normal incidence since its excitation is symmetry forbidden.⁴¹ For the aforementioned symmetry considerations, to excite the MD mode, it is necessary to introduce a phase retardation inside the volume of the cuboids by changing the illumination angle.⁴² The same symmetry rules are applied to the excitation of the MD mode in the co-S polarization at which the MQ mode cannot be excited at any incident angle (see Figure 2d). The corresponding local field distributions for cross-S and co-S polarizations at 4° illumination are shown in Figures S8 and S9. By illuminating the metasurface at both cross-S and co-S polarizations, the Rayleigh anomalies and the broad Fabry–Pérot resonance are clearly resolved in the transmission spectra (see the Supporting Information, Sections 2 and 3). More importantly, MQ and MD modes hybridize with the quasi-BIC mode emerging at larger incident angles. The excitation of the quasi-BIC mode occurs by analogy with its excitation in metasurfaces consisting of an array of rectangular waveguides. The principle of excitation of the quasi-BIC mode in such a metasurface and the corresponding local field distributions are shown in Figures 2e–h and S5–S7. As a result, the emergence of a hybrid mode leads to the redistribution of local electric fields in cuboids.

The quasi-BIC mode is characterized by the presence of dominant $|H_z|$ and $|E_x|$ components; thus, the incident pump field must match those components (see Figure 2e–h). As the H_z component of the incident field remains equal to zero at cross-P and co-P polarizations, the quasi-BIC mode is not excited in the metasurfaces formed by cuboids (see Figure S2c,d) and rectangular waveguides (see Figure S5e,f) and the redistribution of local electric fields inside the cuboids is not observed (see Figure S10). To excite the quasi-BIC mode around 1550 nm and to probe its hybridization with the MQ

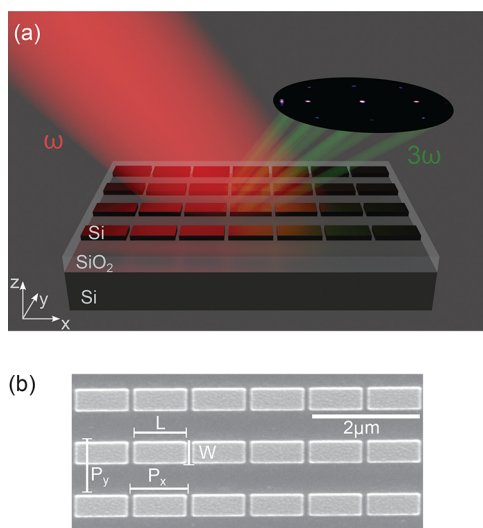


Figure 1. (a) Schematic illustration of our THG experiment. (b) Scanning electron microscopy image of the metasurface. $P_x = 1065$ nm, $P_y = 1060$ nm, $L = 940$ nm, and $W = 428$ nm.

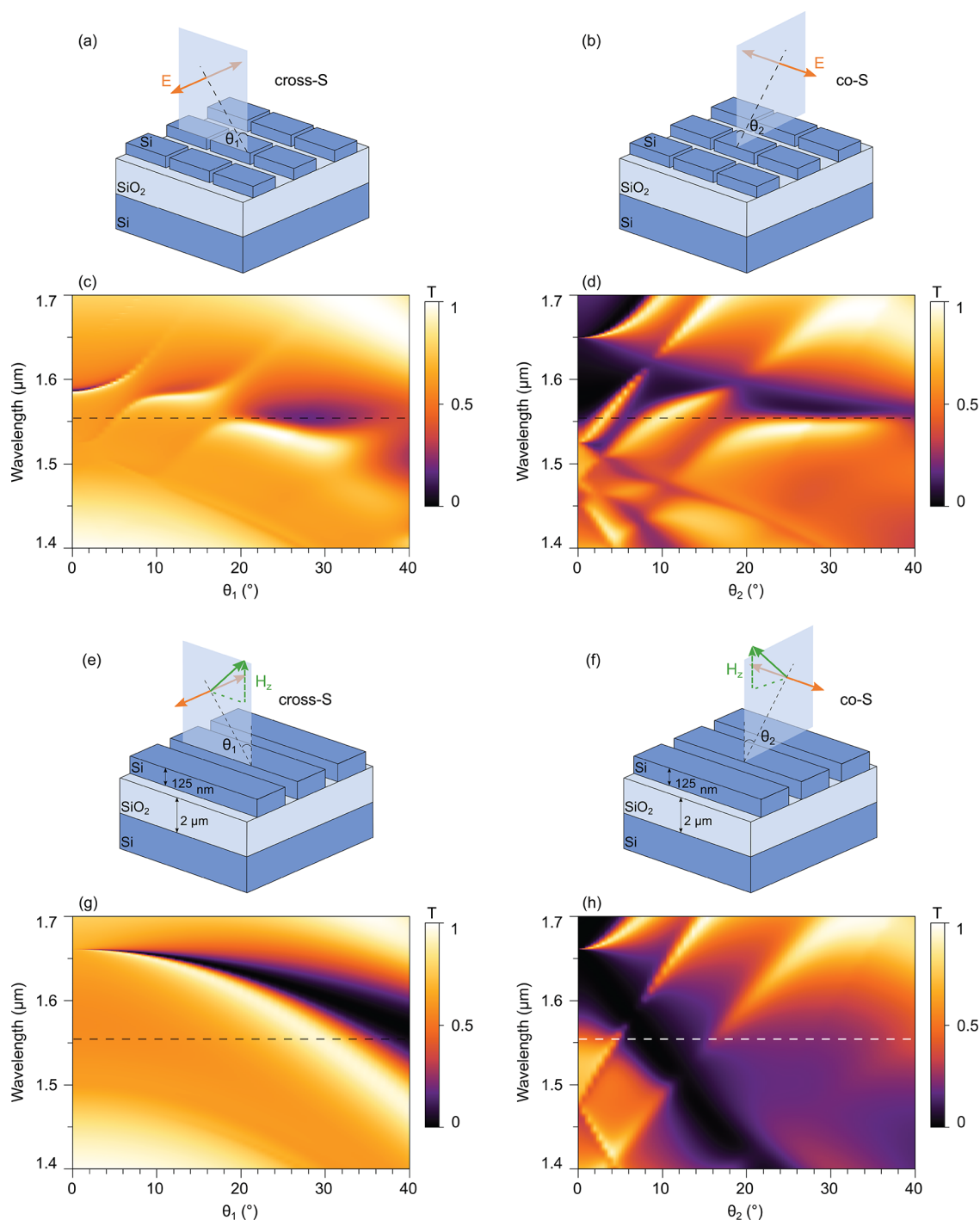


Figure 2. Schematic drawings of cross-S and co-S polarized excitation (a, b) for metasurfaces comprising cuboids and (e, f) for metasurfaces comprising infinite waveguides. Calculated transmittance as a function of the angle and wavelength of incidence for cross-S and co-S polarization (c, d) for metasurfaces comprising cuboids and (g, h) for metasurfaces comprising infinite waveguides. The dashed lines indicate the excitation wavelength of 1554 nm.

and MD Mie-type modes in the nonlinear regime, we further focus on experiments with the cross-S and co-S polarizations.

The metasurface is illuminated by a collimated femtosecond laser beam at different incident angles in cross-S and co-S polarizations. The angle of incidence on the sample is controlled by the movement of the loosely focused beam across the back focal plane of the objective lens (see [BFP Imaging of THG Diffraction Orders](#) and [Figure S1](#)). The output THG signal is collected by the same objective in the

backscattering configuration. The THG diffraction pattern is imaged by a cooled CCD camera. The details of the experimental setup are provided in the [Methods](#) section. Each diffraction order is integrated over the same spatial area, and the signal from the substrate is subtracted. A set of THG diffraction patterns corresponding to different incident angles is obtained. The typical patterns of THG signals that correspond to $(-1,0)$, $(1,0)$, $(0,1)$, and $(0,-1)$ diffraction orders for cross-S polarization at 0° and 22° of incidence are

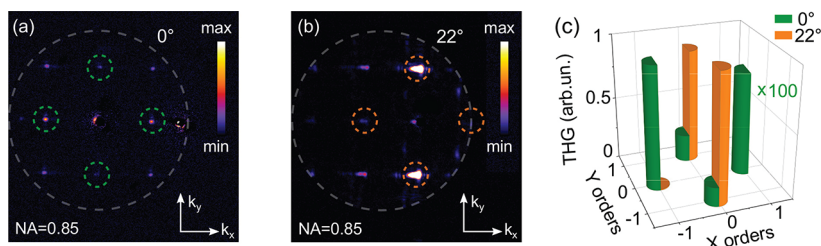


Figure 3. BFP images of the THG diffraction patterns at angles of incidence of 0° (a) and 22° (b) for cross-S exciting polarization. The large dashed gray circles denote the NA of the collecting objective. The small dashed green and orange circles denote the areas where the THG signal was integrated. (c) Power of the THG diffraction orders in panels a (green) and b (orange). THG at 0° (green bars) is magnified 100 times.

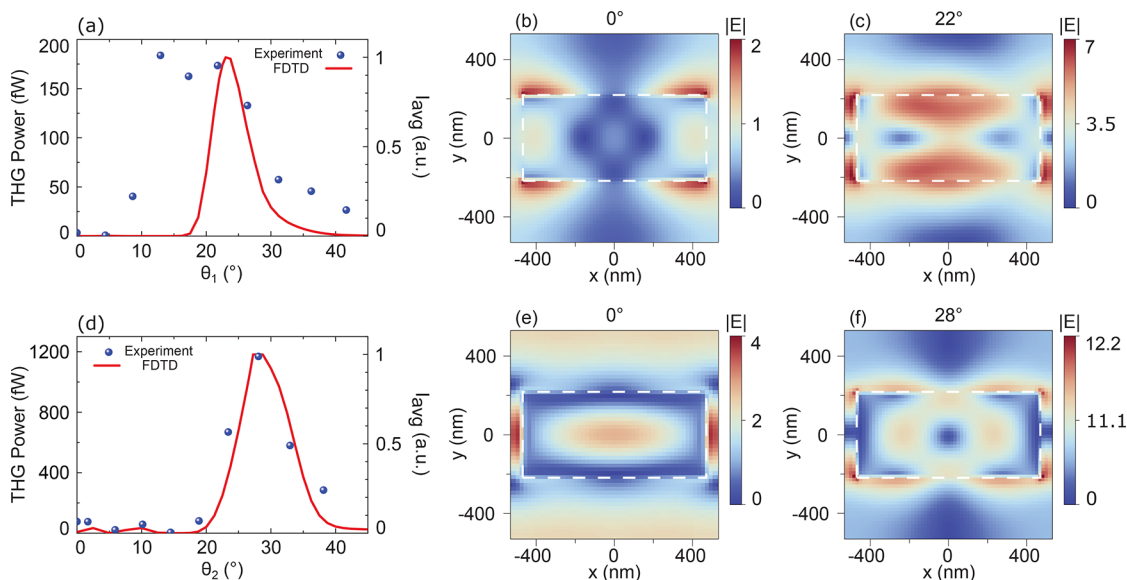


Figure 4. (a, d) Experimental THG signal as a function of the angle of incidence and THG response evaluated from FDTD simulations in cross-S and co-S polarizations, respectively. (b, c) Normalized electric field in the middle of the xy plane of the silicon cuboid at the wavelength of 1554 nm in cross-S excitation at incident angles of 0° and 22° . (e, f) Normalized electric field in the middle of the xy plane of the silicon cuboid at the wavelength of 1554 nm in co-S excitation at incident angles of 0° and 28° . Dashed white rectangles indicate the borders of the cuboids.

shown in Figure 3a,b, where the areas of integration are highlighted by dashed green and orange circles, respectively. The $(1,0)$ diffraction order falls outside the objective collection range at the angle of incidence of 22° due to the angular shift of the THG diffraction map. The integrated signals from these maps are represented in Figure 3c, and the switching from $(\pm 1,0)$ THG diffraction orders for normal incidence to $(0,\pm 1)$ orders for $\theta = 22^\circ$ is clearly seen.

The overall THG is retrieved as the sum of all detected diffraction orders. Its dependence on the angle of incidence is shown in Figure 4a,d in the case of cross-S and co-S polarizations, respectively. The strong enhancements of THG intensities are clearly observed at certain angles for both polarizations. The maximum TH emission of 173 fW is achieved at approximately 20° for cross-S, and the maximum of 1.17 pW is achieved at $\theta = 28^\circ$ for co-S. These experimental THG enhancements are attributed to the local electric field enhancement inside the silicon cuboids at the wavelengths of the hybrid Mie–quasi BIC mode excitation. We estimate the THG efficiency to be 10^{-11} for cross-S polarization and 7×10^{-11} for co-S polarization.

We have performed numerical simulations and integrated the electric field within the volume of the cuboids. A detailed description of the simulations is given in the Supporting Information, Section 6. In Figure 4a,d, we plot the quantity

$$I_{\text{avg}} \propto \int_{\text{volume}} \int_{\text{pulse}} |\mathbf{E}(\mathbf{r}, \nu)|^6 dV d\nu \quad (1)$$

where $\mathbf{E}(\mathbf{r}, \nu)$ is the calculated electric field distribution, and the integrals are performed over the volume of the cuboid and over the spectrum of the laser pulse. Taking into account the electric fields only at the fundamental frequency, we have a good agreement between the experimental and simulated resonant peak angles for THG. The field enhancements are visualized in local electric field distributions in the xy plane through the middle of the cuboid at normal incidence and at the angles corresponding to the maximum signals at 22° for cross-S and at 28° for co-S; see Figure 4b,c,e,f. These electric field maps show the electric field redistribution and their enhancement with respect to normal incidence by a factor of up to 7 and 2.5, respectively.

The studied metasurface is a system for efficient THG and, at the same time, a diffraction grating for the THG light. Typical experimentally obtained THG diffraction patterns are shown in Figure 3a,b with the first diffraction orders occurring at an angle close to $\theta = 30^\circ$ (highlighted with green circles) at the normal pump incidence, as $\text{NA} = \sin \theta = \text{THG wavelength/period} = 518 \text{ nm}/1060 \text{ nm}$. The THG diffraction pattern shifts with a tilt in the incident angle as it is shown in Figure 3b. As the angle of incidence is varied, the redistribution

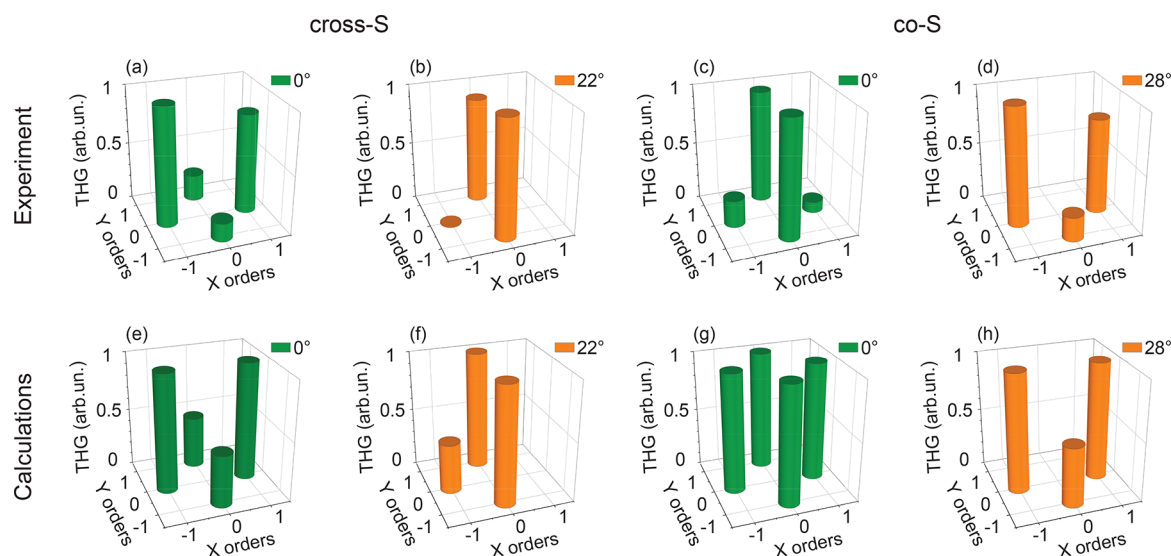


Figure 5. THG power distribution between the diffraction orders. (a, b) Experimental and (e, f) simulated power distribution for cross-S polarization at incident angles of 0° and 22° . (c, d), (g, h) Same as (a, b) and (e, f) for co-S polarization at incident angles of 0° and 28° .

of intensity between diffraction orders is observed. Figure 5a–d represents the experimental THG signals at the $(-1,0)$, $(1,0)$, $(0,1)$, and $(0,-1)$ diffraction orders for both cross-S and co-S polarizations. At normal incidence and cross-S illumination, the brightest THG orders are $(\pm 1,0)$. As the angle of incidence is tilted, the ratio between the intensities of different pairs of diffraction orders changes and redistribution between diffraction orders is achieved at the condition of resonant excitation of the hybrid Mie–quasi-BIC mode at 22° , where the most intense diffraction orders are $(0,\pm 1)$ (see Figure 5b). The opposite behavior is observed in co-S polarization, where $(0,\pm 1)$ orders are the most intense at normal incidence excitation (see Figure 5c,g). However, at the resonance of the hybrid mode at $\theta = 28^\circ$, $(\pm 1,0)$ orders are much brighter than $(0,\pm 1)$ ones.

The observed switching between pairs of THG diffraction orders with a tilt in the angle of incidence is explained by the far field emission of dipole sources at 3ω . The dipoles mimic the hot spots of the electric field in the cuboid cross section on the middle of its height with suitable positions, amplitudes, and phases taken from Figure 4b,c,e,f. We simulate the metasurface response by arranging the dipoles in 2D arrays that correspond to the hot spots of E_x and E_y fields. The dipoles at the THG frequency spatially coincide with the dipoles at the fundamental frequency, and there is a phase shift between dipoles in the case of tilted incidence. A detailed account of how diffraction orders are simulated is given in the Supporting Information, Section 7. The calculated THG diffraction order bar diagrams are in good agreement with the experimental ones where the most intense orders for cross-S are $(\pm 1,0)$ at normal incidence and $(0,\pm 1)$ at 22° incidence (see Figure 5). All four calculated THG diffraction orders have comparable intensities with slightly larger values for $(0,\pm 1)$ orders at co-S polarization at normal incidence. The mismatch between calculations and experiment is possibly due to the fact that the model deals with point sources rather than the extended sources of local field as it is shown in the electric field map in Figure 4e. The simulations are in excellent agreement with the experimental THG diffraction orders for co-S polarization at the resonant excitation corresponding to a 28° incidence angle. It can be concluded that the redistribution between the THG

diffraction orders with a tilted angle of incidence occurs due to the changes in the arrangement of the electric dipoles in the metasurface caused by the excitation of the hybrid Mie–quasi-BIC mode in cross-S and co-S polarizations.

In summary, we experimentally demonstrate the intensity switching between THG diffraction orders in a high-Q resonant silicon metasurface. This phenomenon is associated with the excitation of the hybrid Mie–quasi-BIC mode at the oblique incidence of the laser beam that results in the enhancement and the spatial redistribution of local electric fields inside the elements of the metasurface. These modifications in the local electric field distributions observed for two cases of incident linear polarizations lead to changes in the far-field THG diffraction pattern. This correlation between near-field and far-field distributions is well described by a simulation model based on local nonlinear dipole sources. Our results pave the way to efficient nonlinear wavefront control by all-dielectric metasurfaces.

METHODS

Sample Fabrication. The metasurface was fabricated using a silicon-on-insulator (SOI) (001) wafer with a device thickness of 125 nm and a box of $2 \mu\text{m}$. The (110) orientation of silicon lattice was aligned along the long side of the fabricated cuboids. Two layers of positive PMMA resist with a final thickness of ~ 200 nm were spin-coated on the SOI, which was patterned via the electron-beam lithography (EBL) to define the desired patterns. During the lithographic step, different doses were used to create cuboids with a length of 940 nm (± 10 nm), width of 428 nm (± 10 nm), and spatial period of 1060 nm. The regular pattern in the SOI was obtained by reactive-ion etching (RIE) using CF_4 as the etchant gas (Figure 1b). A more detailed description of the fabrication process is provided in ref 39. The RIE etching rate was adjusted to etch 125 nm of the Si device layer, and the etch depth was characterized with atomic force microscopy (AFM) and scanning electron microscopy (SEM). The final removal of the resist was carried out with 10 min of acetone and isopropanol cleaning; this wet-chemical step may leave resist residues, which were therefore removed by a 225 W

oxygen plasma system and a 5 s HF rinse (5% vol). In particular, the use of the hot acetone is specific for the removal of the surface organic contamination that could be derived from the lithography process. To completely remove any residual resist, the samples were cleaned in an oxygen atmosphere in a plasma Asher system by a combustion process. Finally, a quick passage in diluted HF removed any surface contamination trapped in the native oxide formed on the silicon surface without any measurable damage of the BOX.⁴³

BFP Imaging of THG Diffraction Orders. We employ back focal plane (BFP) imaging in reflectance accompanied by THG microscopy for measurements of the THG diffraction patterns. The scheme of the experimental setup is shown in Figure S1. The radiation of a femtosecond laser (oneFive, Origami-15) with a central wavelength of 1554 nm, 160 fs pulse duration, and 80 MHz repetition rate was loosely focused onto the BFP of the objective by a 50 cm-focal length doublet (ThorLabs, AC254-300-C-ML) to uniformly illuminate the $25 \times 25 \mu\text{m}^2$ area of the sample. The 60 \times objective lens with an NA of 0.85 (Nikon, Plan Fluorite) formed a quasi collimated beam with an fwhm of approximately the size of the metasurface and, at the same time, collected the THG signal in a backscattering configuration. A dichroic mirror (ThorLabs, DMLP950) was placed before the objective to separate the fundamental beam and the nonlinear emission. Sample was placed on an *xyz*-piezo stage facing the incident radiation. Two confocal lenses with focal lengths of 50 and 40 cm, respectively, were mounted in the detection path to image the BFP of the objective. The second lens relayed the BFP image onto the sensor of a cooled CCD camera (Andor, iKon-M). Bandpass (ThorLabs, FBH520-40) and shortpass (ThorLabs, FESH0700) filters were inserted in the detection path for chromatic filtering of the THG at a wavelength of 518 nm. The linear polarization of the pump beam was controlled by a half wave retarder. The oblique incidence of the quasi collimated beam on the sample was realized by laterally shifting the loosely focused beam across the BFP of the objective.

■ ASSOCIATED CONTENT

SI Supporting Information

The Supporting Information is available free of charge at <https://pubs.acs.org/doi/10.1021/acs.nanolett.1c03790>.

Scheme of experimental setup of THG microscopy; calculations of angle-resolved transmittance spectra for cross-P and co-P polarizations; calculations of Fabry-Pérot resonance in three-layer structure Si-SiO₂-Si and Rayleigh anomalies in the metasurface; calculations of angle-resolved transmittance spectra for cross-S, co-S, cross-P, and co-P polarizations and local electric field localization in the metasurface from infinite waveguides; calculations of local electric field localization for cross-S, co-S, cross-P, and co-P polarizations in the metasurface; experimental and simulated THG diffraction maps for cross-P and co-P polarizations for the metasurface; description of FDTD simulations and simulations of THG diffraction maps; calculations of linear diffraction from metasurfaces at 3ω frequency; experimental THG diffraction maps for cross-S and co-S polarizations for the metasurface with close to equal first diffraction orders; calculations of angular-resolved transmittance

spectra for metasurfaces without substrates; processing of raw BFP images of THG patterns (PDF)

■ AUTHOR INFORMATION

Corresponding Author

Kirill I. Okhlopov – Faculty of Physics, Lomonosov Moscow State University, 119991 Moscow, Russia;
Email: okhlopov@nanolab.phys.msu.ru

Authors

Attilio Zilli – Department of Physics, Politecnico di Milano, 20133 Milano, Italy; orcid.org/0000-0003-1845-6850
Andrea Tognazzi – Department of Information Engineering, University of Brescia, 25123 Brescia, Italy; CNR-INO (National Institute of Optics), 25123 Brescia, Italy
Davide Rocco – Department of Information Engineering, University of Brescia, 25123 Brescia, Italy; CNR-INO (National Institute of Optics), 25123 Brescia, Italy
Luca Fagiani – Department of Physics, Politecnico di Milano, 20133 Milano, Italy; CNR-IFN, LNESS Laboratory, 22100 Como, Italy
Erfan Mafakheri – CNR-IFN, LNESS Laboratory, 22100 Como, Italy
Monica Bollani – CNR-IFN, LNESS Laboratory, 22100 Como, Italy
Marco Finazzi – Department of Physics, Politecnico di Milano, 20133 Milano, Italy; orcid.org/0000-0002-9197-3654
Michele Celebrano – Department of Physics, Politecnico di Milano, 20133 Milano, Italy; orcid.org/0000-0003-3336-3580
Maxim R. Shcherbakov – Faculty of Physics, Lomonosov Moscow State University, 119991 Moscow, Russia; Department of Electrical Engineering and Computer Science, University of California, Irvine, California 92697, United States; orcid.org/0000-0001-7198-5482
Costantino De Angelis – Department of Information Engineering, University of Brescia, 25123 Brescia, Italy; CNR-INO (National Institute of Optics), 25123 Brescia, Italy; orcid.org/0000-0001-8029-179X
Andrey A. Fedyanin – Faculty of Physics, Lomonosov Moscow State University, 119991 Moscow, Russia; orcid.org/0000-0003-4708-6895

Complete contact information is available at:
<https://pubs.acs.org/doi/10.1021/acs.nanolett.1c03790>

Notes

The authors declare no competing financial interest.

■ ACKNOWLEDGMENTS

The work was performed under financial support of the Russian Ministry of Education and Science (Grant No. 14.W03.31.0008, numerical calculations) and the Russian Foundation for Basic Research (Grant No. 21-52-12036, sample characterization). K.I.O. thanks MSU Quantum Technology Centre for the support. M.R.S. thanks the Russian Science Foundation (Grant No. 18-12-00475, optical measurements). A.A.F. thanks the Interdisciplinary Scientific and Educational School of Lomonosov Moscow State University, “Photonic and Quantum technologies. Digital medicine”. Part of the work was supported by the European Commission (828890 (FET Open NARCISO), 899673 (FET Open

METAFAST)); Ministero dell'Istruzione, dell'Università e della Ricerca (2017MP7F8F (PRIN project NOMEN)).

REFERENCES

- (1) Freund, I. Nonlinear diffraction. *Phys. Rev. Lett.* **1968**, *21*, 1404.
- (2) Berger, V. Nonlinear photonic crystals. *Phys. Rev. Lett.* **1998**, *81*, 4136.
- (3) Peng, L.-H.; Hsu, C.-C.; Shih, Y.-C. Second-harmonic green generation from two-dimensional $\chi^{(2)}$ nonlinear photonic crystal with orthorhombic lattice structure. *Appl. Phys. Lett.* **2003**, *83*, 3447–3449.
- (4) Saltiel, S. M.; Neshev, D. N.; Fischer, R.; Krolikowski, W.; Arie, A.; Kivshar, Y. S. Generation of second-harmonic conical waves via nonlinear Bragg diffraction. *Phys. Rev. Lett.* **2008**, *100*, 103902.
- (5) Fedyanin, A. A.; Aktsipetrov, O. A.; Kurdyukov, D. A.; Golubev, V. G.; Inoue, M. Nonlinear diffraction and second-harmonic generation enhancement in silicon-opal photonic crystals. *Appl. Phys. Lett.* **2005**, *87*, 151111.
- (6) Soboleva, I. V.; Seregin, S. A.; Fedyanin, A. A.; Aktsipetrov, O. A. Efficient bidirectional optical harmonics generation in three-dimensional photonic crystals. *J. Opt. Soc. Am. B* **2011**, *28*, 1680–1684.
- (7) Yu, Y. F.; Zhu, A. Y.; Paniagua-Domínguez, R.; Fu, Y. H.; Luk'yanchuk, B.; Kuznetsov, A. I. High-transmission dielectric metasurface with 2π phase control at visible wavelengths. *Laser & Photonics Reviews* **2015**, *9*, 412–418.
- (8) Pors, A.; Albrechtsen, O.; Radko, I. P.; Bozhevolnyi, S. I. Gap plasmon-based metasurfaces for total control of reflected light. *Sci. Rep.* **2013**, *3*, 2155.
- (9) Qin, F.; Ding, L.; Zhang, L.; Monticone, F.; Chum, C. C.; Deng, J.; Mei, S.; Li, Y.; Teng, J.; Hong, M.; et al. Hybrid bilayer plasmonic metasurface efficiently manipulates visible light. *Science Advances* **2016**, *2*, No. e1501168.
- (10) Lin, D.; Fan, P.; Hasman, E.; Brongersma, M. L. Dielectric gradient metasurface optical elements. *Science* **2014**, *345*, 298–302.
- (11) Wang, L.; Kruk, S.; Tang, H.; Li, T.; Kravchenko, I.; Neshev, D. N.; Kivshar, Y. S. Grayscale transparent metasurface holograms. *Optica* **2016**, *3*, 1504–1505.
- (12) Song, X.; Huang, L.; Tang, C.; Li, J.; Li, X.; Liu, J.; Wang, Y.; Zentgraf, T. Selective diffraction with complex amplitude modulation by dielectric metasurfaces. *Adv. Opt. Mater.* **2018**, *6*, 1701181.
- (13) Komar, A.; Paniagua-Domínguez, R.; Miroshnichenko, A.; Yu, Y. F.; Kivshar, Y. S.; Kuznetsov, A. I.; Neshev, D. N. Dynamic beam switching by liquid crystal tunable dielectric metasurfaces. *ACS Photonics* **2018**, *5*, 1742–1748.
- (14) Ghirardini, L.; Malerba, M.; Bollani, M.; Biagioni, P.; Duo, L.; Finazzi, M.; De Angelis, F.; Celebrano, M. Nonlinear emission from silver-coated 3D hollow nanopillars. *Nanospectroscopy* **2016**, *2*, 15–23.
- (15) Shcherbakov, M. R.; Neshev, D. N.; Hopkins, B.; Shorokhov, A. S.; Staude, I.; Melik-Gaykazyan, E. V.; Decker, M.; Ezhov, A. A.; Miroshnichenko, A. E.; Brener, I.; et al. Enhanced third-harmonic generation in silicon nanoparticles driven by magnetic response. *Nano Lett.* **2014**, *14*, 6488–6492.
- (16) Shcherbakov, M. R.; Vabishchevich, P. P.; Shorokhov, A. S.; Chong, K. E.; Choi, D.-Y.; Staude, I.; Miroshnichenko, A. E.; Neshev, D. N.; Fedyanin, A. A.; Kivshar, Y. S. Ultrafast all-optical switching with magnetic resonances in nonlinear dielectric nanostructures. *Nano Lett.* **2015**, *15*, 6985–6990.
- (17) Yang, Y.; Wang, W.; Boulesbaa, A.; Kravchenko, I. I.; Briggs, D. P.; Puzetky, A.; Geohagan, D.; Valentine, J. Nonlinear Fano-resonant dielectric metasurfaces. *Nano Lett.* **2015**, *15*, 7388–7393.
- (18) Liu, S.; Sinclair, M. B.; Saravi, S.; Keeler, G. A.; Yang, Y.; Reno, J.; Peake, G. M.; Setzpfandt, F.; Staude, I.; Pertsch, T.; et al. Resonantly enhanced second-harmonic generation using III–V semiconductor all-dielectric metasurfaces. *Nano Lett.* **2016**, *16*, 5426–5432.
- (19) Toliopoulos, D.; Khoury, M.; Bouabdellaoui, M.; Granchi, N.; Claude, J.-B.; Benali, A.; Berbezier, I.; Hannani, D.; Ronda, A.; Wenger, J.; et al. Fabrication of spectrally sharp Si-based dielectric resonators: combining etaloning with Mie resonances. *Opt. Express* **2020**, *28*, 37734–37742.
- (20) Okhlopkov, K. I.; Shafirin, P. A.; Ezhov, A. A.; Orlikovsky, N. A.; Shcherbakov, M. R.; Fedyanin, A. A. Optical coupling between resonant dielectric nanoparticles and dielectric nanowires probed by third harmonic generation microscopy. *ACS Photonics* **2019**, *6*, 189–195.
- (21) Kroychuk, M. K.; Shorokhov, A. S.; Yagudin, D. F.; Shilkin, D. A.; Smirnova, D. A.; Volkovskaya, I.; Shcherbakov, M. R.; Shvets, G.; Fedyanin, A. A. Enhanced nonlinear light generation in oligomers of silicon nanoparticles under vector beam illumination. *Nano Lett.* **2020**, *20*, 3471–3477.
- (22) Walter, F.; Li, G.; Meier, C.; Zhang, S.; Zentgraf, T. Ultrathin nonlinear metasurface for optical image encoding. *Nano Lett.* **2017**, *17*, 3171–3175.
- (23) Gao, Y.; Fan, Y.; Wang, Y.; Yang, W.; Song, Q.; Xiao, S. Nonlinear holographic all-dielectric metasurfaces. *Nano Lett.* **2018**, *18*, 8054–8061.
- (24) Reineke, B.; Sain, B.; Zhao, R.; Carletti, L.; Liu, B.; Huang, L.; De Angelis, C.; Zentgraf, T. Silicon metasurfaces for third harmonic geometric phase manipulation and multiplexed holography. *Nano Lett.* **2019**, *19*, 6585–6591.
- (25) Wang, L.; Kruk, S.; Koshelev, K.; Kravchenko, I.; Luther-Davies, B.; Kivshar, Y. Nonlinear wavefront control with all-dielectric metasurfaces. *Nano Lett.* **2018**, *18*, 3978–3984.
- (26) Löchner, F. J.; Fedotova, A. N.; Liu, S.; Keeler, G. A.; Peake, G. M.; Saravi, S.; Shcherbakov, M. R.; Burger, S.; Fedyanin, A. A.; Brener, I.; et al. Polarization-dependent second harmonic diffraction from resonant GaAs metasurfaces. *ACS Photonics* **2018**, *5*, 1786–1793.
- (27) Fedotova, A.; Younesi, M.; Sautter, J.; Vaskin, A.; Löchner, F. J.; Steinert, M.; Geiss, R.; Pertsch, T.; Staude, I.; Setzpfandt, F. Second-Harmonic Generation in Resonant Nonlinear Metasurfaces Based on Lithium Niobate. *Nano Lett.* **2020**, *20*, 8608–8614.
- (28) Carletti, L.; Zilli, A.; Moia, F.; Toma, A.; Finazzi, M.; De Angelis, C.; Neshev, D. N.; Celebrano, M. Steering and encoding the polarization of the second harmonic in the visible with a monolithic LiNbO₃ metasurface. *ACS Photonics* **2021**, *8*, 731–737.
- (29) Kuznetsov, A. I.; Miroshnichenko, A. E.; Brongersma, M. L.; Kivshar, Y. S.; Luk'yanchuk, B. Optically resonant dielectric nanostructures. *Science* **2016**, *354*, 1.
- (30) Hsu, C. W.; Zhen, B.; Lee, J.; Chua, S.-L.; Johnson, S. G.; Joannopoulos, J. D.; Soljačić, M. Observation of trapped light within the radiation continuum. *Nature* **2013**, *499*, 188–191.
- (31) Hsu, C. W.; Zhen, B.; Stone, A. D.; Joannopoulos, J. D.; Soljačić, M. Bound states in the continuum. *Nature Reviews Materials* **2016**, *1*, 16048.
- (32) Carletti, L.; Koshelev, K.; De Angelis, C.; Kivshar, Y. Giant nonlinear response at the nanoscale driven by bound states in the continuum. *Phys. Rev. Lett.* **2018**, *121*, 033903.
- (33) Koshelev, K.; Kruk, S.; Melik-Gaykazyan, E.; Choi, J.-H.; Bogdanov, A.; Park, H.-G.; Kivshar, Y. Subwavelength dielectric resonators for nonlinear nanophotonics. *Science* **2020**, *367*, 288–292.
- (34) Shcherbakov, M. R.; Werner, K.; Fan, Z.; Talisa, N.; Chowdhury, E.; Shvets, G. Photon acceleration and tunable broadband harmonics generation in nonlinear time-dependent metasurfaces. *Nat. Commun.* **2019**, *10*, 1345.
- (35) Lawrence, M.; Barton, D. R.; Dixon, J.; Song, J.-H.; van de Groep, J.; Brongersma, M. L.; Dionne, J. A. High quality factor phase gradient metasurfaces. *Nat. Nanotechnol.* **2020**, *15*, 956–961.
- (36) Limonov, M. F.; Rybin, M. V.; Poddubny, A. N.; Kivshar, Y. S. Fano resonances in photonics. *Nat. Photonics* **2017**, *11*, 543–554.
- (37) Malek, S. C.; Overvig, A. C.; Shrestha, S.; Yu, N. Active nonlocal metasurfaces. *Nanophotonics* **2020**, *10*, 655–665.
- (38) Tognazzi, A.; Okhlopkov, K. I.; Zilli, A.; Rocco, D.; Fagiani, L.; Mafakheri, E.; Bollani, M.; Finazzi, M.; Celebrano, M.; Shcherbakov, M. R.; et al. Third-harmonic light polarization control in magnetically resonant silicon metasurfaces. *Opt. Express* **2021**, *29*, 11605–11612.
- (39) Fagiani, L.; Zilli, A.; Tognazzi, A.; Mafakheri, E.; Okhlopkov, K. I.; Rocco, D.; Shcherbakov, M. R.; Fedyanin, A. A.; De Angelis, C.; Finazzi, M.; Celebrano, M.; Bollani, M. Silicon metasurfaces with

tunable electromagnetic resonances for nonlinear optical conversion.

Il Nuovo Cimento C **2021**, *44*, 1–4.

(40) Martemyanov, M.; Kim, E.; Dolgova, T.; Fedyanin, A.; Aktsipetrov, O.; Marowsky, G. Third-harmonic generation in silicon photonic crystals and microcavities. *Phys. Rev. B: Condens. Matter Mater. Phys.* **2004**, *70*, 073311.

(41) Frolov, A. Y.; Verellen, N.; Li, J.; Zheng, X.; Paddubrouskaya, H.; Denkova, D.; Shcherbakov, M. R.; Vandenbosch, G. A.; Panov, V. I.; Van Dorpe, P.; et al. Near-field mapping of optical Fabry–Perot modes in all-dielectric nanoantennas. *Nano Lett.* **2017**, *17*, 7629–7637.

(42) Traviss, D. J.; Schmidt, M. K.; Aizpurua, J.; Muskens, O. L. Antenna resonances in low aspect ratio semiconductor nanowires. *Opt. Express* **2015**, *23*, 22771–22787.

(43) Bollani, M.; Salvalaglio, M.; Benali, A.; Bouabdellaoui, M.; Naffouti, M.; Lodari, M.; Di Corato, S.; Fedorov, A.; Voigt, A.; Fraj, I.; et al. Templated dewetting of single-crystal sub-millimeter-long nanowires and on-chip silicon circuits. *Nat. Commun.* **2019**, *10*, 5632.